

# Accepted Manuscript

Building block nanoparticles engineering induces multi-element perovskite hollow nanofibers structure evolution to trigger enhanced oxygen evolution

Meng Wan, Han Zhu, SongGe Zhang, HaoNan Jin, YanKun Wen, Lina Wang, Ming Zhang, MingLiang Du



PII: S0013-4686(18)31110-1

DOI: [10.1016/j.electacta.2018.05.077](https://doi.org/10.1016/j.electacta.2018.05.077)

Reference: EA 31863

To appear in: *Electrochimica Acta*

Received Date: 27 February 2018

Revised Date: 8 May 2018

Accepted Date: 12 May 2018

Please cite this article as: M. Wan, H. Zhu, S. Zhang, H. Jin, Y. Wen, L. Wang, M. Zhang, M. Du, Building block nanoparticles engineering induces multi-element perovskite hollow nanofibers structure evolution to trigger enhanced oxygen evolution, *Electrochimica Acta* (2018), doi: 10.1016/j.electacta.2018.05.077.

This is a PDF file of an unedited manuscript that has been accepted for publication. As a service to our customers we are providing this early version of the manuscript. The manuscript will undergo copyediting, typesetting, and review of the resulting proof before it is published in its final form. Please note that during the production process errors may be discovered which could affect the content, and all legal disclaimers that apply to the journal pertain.

**Building block nanoparticles engineering induces multi-element Perovskite hollow nanofibers structure evolution to trigger enhanced oxygen evolution**

*Meng Wan<sup>1</sup>, Han Zhu<sup>1,2\*</sup>, SongGe Zhang<sup>1,2</sup>, HaoNan Jin<sup>1</sup>, YanKun Wen<sup>1,2</sup>, Lina Wang<sup>1</sup>, Ming Zhang<sup>1</sup>, MingLiang Du<sup>1,2\*</sup>*

<sup>1</sup> College of Materials and Textiles, Zhejiang Sci-Tech University, Hangzhou, 310018, P. R. China

<sup>2</sup> Key Laboratory of Synthetic and Biological Colloids, Ministry of Education, School of Chemical and Material Engineering, Jiangnan University, Wuxi 214122, P. R. China

E-mail: zhysw@jiangnan.edu.cn; du@jiangnan.edu.cn

Keywords: Perovskite oxides, hollow nanofibers, Ostwald ripening approach, oxygen evolution reaction

**ABSTRACT:** Oxygen evolution reaction (OER) plays an important role in various renewable energy systems. Owing to its complex four-electron redox process, the OER process with sluggish kinetics often requires electrocatalysts to reduce the overpotential and promote the reaction rate. Herein, we have proposed an “all-in-one” strategy to synthesize multi-elemental perovskite oxides nanofibers (NFs) with hollow and porous structures by using electrospinning technology and Ostwald ripening approach. The hollow  $\text{La}_{0.7}\text{Sr}_{0.3}\text{Co}_{0.25}\text{Mn}_{0.75}\text{O}_3$  nanofibers (LSCM NFs) consist of large amounts of building block  $\text{La}_{0.7}\text{Sr}_{0.3}\text{Co}_{0.25}\text{Mn}_{0.75}\text{O}_3$  nanoparticles (LSCM NPs), forming the unique architecture and the morphologies can be engineering by

adjusting the calcination temperatures and the heating rates. Notably, the hollow LSCM NFs prepared at 800 °C and 10 °C min<sup>-1</sup> demonstrated the excellent electrocatalytic performance, with overpotential of 340 mV at current density of 10 mA cm<sup>-2</sup> and Tafel slope of 111 mV dec<sup>-1</sup>, as well as the long-term stability in alkaline electrolyte. The hollow NFs architectures exhibited a large specific surface area, a high porosity and a large inner space, which are beneficial for the OER, reducing the overpotentials and accelerating the electrode kinetics.

## 1. Introduction

Energy shortage and environmental pollution have become two serious issues due to the overuse of fossil fuels. In recent years, more and more efforts have been devoted to develop the sustainable and clean energy, aiming to replace the fossil fuels [1-3]. Hydrogen energy is a desirable and alternative energy with three important merits: high heat of combustion, non-pollution and abundant resources. Hydrogen energy can be obtained from water through the electrocatalysis or the photocatalysis approaches [4-9]. Electrocatalytic water splitting is considered as a remarkable technique to produce hydrogen and the electrolysis of water involves double half-reaction: hydrogen evolution reaction (HER,  $2\text{H}_2\text{O} \rightarrow \text{H}_2 + 2\text{OH}^- - 4\text{e}^-$ ) and oxygen evolution reaction (OER,  $2\text{H}_2\text{O} \rightarrow \text{O}_2 + 4\text{H}^+ + 4\text{e}^-$ ) [10-13]. More importantly, the OER process combining four-electron transfer with sluggish kinetics is the pivotal step for hydrogen generation. In addition, in the process of alkaline water electrolysis, the anodic anode usually requires high activation overpotential [14,15]. Nowadays, the state-of-the-art electrocatalyst for OER are iridium or ruthenium oxide (IrO<sub>2</sub> or RuO<sub>2</sub>), and however, the large-scale applications were hindered due to their high-cost and scarcity [16,17]. Therefore, it is imperative to exploit advanced and earth-abundant OER catalysts with high activity and stability to significantly decrease the overpotential for OER, further improving the efficiency of water splitting [18-20].

Over the past few years, the earth-abundant transition metal oxides such as  $\text{MnO}_2$  [21],  $\text{Co}_3\text{O}_4$  [22-25],  $\text{NiCo}_2\text{O}_4$  [25-27],  $\text{MnCo}_2\text{O}_4$  [28-30] are regarded as potential OER catalysts owing to their structural stability, resistance to electrolytic corrosion and high activity. Currently, it is reported that the perovskite oxides are attractive catalysts for oxygen related reactions owing to their high  $\text{OH}^-$  adsorption capability and good  $\text{O}^{2-}$  transfer abilities. The general formula of the perovskite structure is  $\text{ABO}_3$ . A-site represents the alkali metal ions, alkaline earth metal ions or rare earth metal ions while B-site represents the transition metal ions [31,32]. The stoichiometry of oxygen in the perovskite crystal structure is usually different from the nominal value 3 of the formula  $\text{ABO}_3$ . In the previous reported, the bulk perovskite oxides represent certain catalytic activity due to their high ionic, electronic conductivities and structural stabilities. Chen *et al.* have introduced investigation of the OER mechanism of perovskite oxides by ab initio analysis based on well-defined model systems of  $\text{LaMnO}_3$  (LMO),  $\text{LaCoO}_3$  (LCO), and  $\text{La}_{0.5}\text{Sr}_{0.5}\text{CoO}_3$  (LSCO). In addition, they have systematically conducted electrochemical experiments from which we have observed an increasing trend in the OER activity in the order of  $\text{LSCO} > \text{LCO} > \text{LMO}$  in the alkaline medium [33]. The catalytic activity of these bulk perovskite oxides could be further enhanced by decreasing their particles sizes via ball milling or developing novel pore structures. For example, Shao *et al.* have enhanced performance of  $\text{Ba}_{0.5}\text{Sr}_{0.5}\text{Co}_{0.8}\text{Fe}_{0.2}\text{O}_{3-\delta}$  (BSCF) for the OER with intrinsic activity that is significantly higher than that of the benchmark  $\text{IrO}_2$ . And their low specific surface area is the main obstacle to realizing a high mass-specific activity that is required to be competitive against the state-of-the-art precious metal-based catalysts [34]. But the strategy for controlling the structure of the complex perovskite with various metal ions is scarce [35-40]. Exploiting hollow nanostructure with large specific surface area can provide a higher density of surface-exposed active sites and defect-rich porous structure

to improve the mobility and diffusion of the charges [41-44]. However, it remains challenges to develop a simple and direct method to obtain hollow perovskite NFs with controllable nanostructures.

Herein, we reported a facile strategy for the synthesis of multi-element hollow perovskite oxides NFs with controllable tubular structure and morphology by combining the electrospinning technology and Ostwald ripening approach. Inorganic oxides hollow nanofibers are acquired by combining the electrospinning technique and Ostwald ripening approach in the previous reports, which might be owing to the competition between the evaporation rate and the process of phase separation. It should be noted that this kind of the hollow nanofibers can be further tuned by changing the heating treatment conditions [30,45]. The multi-element LSCM NFs consist of large amounts of building block NPs, forming the unique architectures. The building block NPs can be adjusted by changing the calcination temperatures and the heating rates, further determining the tubular structures. It is indicated that higher temperatures and faster heating rates both result in the enlarger of building block NPs, leading to the shrinkage in tubular diameter. The OER performance in correlation with the hollow LSCM NFs with different morphologies and structures has been investigated. The LSCM NFs prepared at 800 °C with heating rate of 10 °C min<sup>-1</sup> exhibits the excellent OER activity with overpotential of 340 mV (10 mA cm<sup>-2</sup>) and Tafel slope of 111 mV dec<sup>-1</sup>. The results demonstrate that the perovskite oxides LSCM NFs are promising electrocatalysts for OER.

## 2. Experimental Methods

### 2.1 Chemicals and Materials

Lanthanum nitrate hexahydrate (LaN<sub>3</sub>O<sub>9</sub>·6H<sub>2</sub>O, 99.9 %), strontium acetate (C<sub>4</sub>H<sub>6</sub>O<sub>4</sub>Sr, AR, 99.0 %), cobalt nitrate hexahydrate (Co(NO<sub>3</sub>)<sub>2</sub>·6H<sub>2</sub>O, AR, 99.0 %), manganese acetate

tetrahydrate ( $\text{MnC}_4\text{H}_6\text{O}_4 \cdot 4\text{H}_2\text{O}$ , AR, 99.0 %) and polyvinylpyrrolidone (PVP,  $(\text{C}_6\text{H}_9\text{NO})_n$ ,  $M_w \approx 1.3 \times 10^6$ ) were commercially available from Shanghai Aladdin Biochemical Technology Co., Ltd. Ethanol ( $\text{C}_2\text{H}_6\text{O}$ , 99.7 %) were purchased from Hangzhou Gaojing Fine Chemical Industry Co., Ltd. All of the chemicals were used without further purification. Deionized water (DIW, 18.2  $\text{M}\Omega$ ) was used for all solution preparations.

### 2.2 Preparation of the LaSrCoMn/PVP nanofibers (LSCM/PVP NFs)

Briefly, 0.285 g  $\text{LaN}_3\text{O}_9 \cdot 6\text{H}_2\text{O}$ , 0.285 g  $\text{C}_4\text{H}_6\text{O}_4\text{Sr}$ , 0.285 g  $\text{Co}(\text{NO}_3)_2 \cdot 6\text{H}_2\text{O}$  and 0.285 g  $\text{MnC}_4\text{H}_6\text{O}_4 \cdot 4\text{H}_2\text{O}$  was added into 2 mL DIW to get a homogeneous solution. Then, 3 g PVP powder, 13.5 mL DIW and 13.5 mL ethanol were mixed into the above solution and magnetic stirred for 24 h to get a homogenous solution. The precursor solution was transferred into a syringe with a stainless copper needle at the tip. The needle was connected to a high voltage power supply. The applied voltage was 12 kV. The distance between needle and collector was 12 cm. The flow rate of the solution was 0.6 mL/h. All experiments were performed at room temperature.

### 2.3 Preparation for the hollow LSCM NFs

The as-collected LSCM/PVP NFs were placed in a ceramic boat and calcined into a home-built furnace with different temperatures (400 °C-1000 °C) in air at a rate of 2 °C  $\text{min}^{-1}$  and maintained for 3 h. Then the samples were cooled to room temperature. In addition, the structures and morphologies of the LSCM NFs obtained at different heating rates were also investigated.

### 2.4 Materials Characterization

The morphologies and structure of the as-prepared were determined by using the field-emission scanning electron microscopy (FE-SEM, JSM-6700F, JEOL, Japan) at an acceleration voltage of 3 kV, transmission electron microscopy (TEM, JSM-2100, JEOL, Japan) at an

acceleration voltage of 200 kV, high-angle annular dark-field scanning transmission electron microscopy (HAADF-STEM, Tecnai G2F30S-Twin, Philips-FEI) at an acceleration voltage of 300 kV. The chemical states and the structure of the LSCM NFs were analyzed by X-ray diffraction (XRD) and X-ray photoelectron spectrometry (XPS). The XRD patterns were recorded using a Breker AXSD8 DISCOVER X-ray diffraction with Cu K $\alpha$  radiation ( $\lambda = 1.5406$  Å, scanning rate is  $0.022 \theta \text{ s}^{-1}$  and  $2 \theta$  range is  $10\text{-}80^\circ$ ). The X-ray photoelectron spectra were analyzed by Kratos Axis Ultra DLD X-ray photoelectron spectrometry at 15 kV and 10 mA with an Al (momo) K $\alpha$  source (1486.6 eV). The fourier transform infrared spectrometer spectra were tested by Fourier transform infrared spectrometer (FT-IR, Nicolet 5700). Thermogravimetric Analysis-Differential Thermal Analysis-Differential Scanning Calorimetry (TG-DTA-DSC, Labsys Evo) were used to get the TG curve measured from room temperature to  $1000^\circ\text{C}$  in the air.

### *2.5 Electrode Preparation*

The nickel foam needs pre-treatment, soaking in the hydrochloric acid solution with the concentration of 24 % for 3 h and washing with the DIW until neutral. The as-prepared LSCM NFs were mixed with acetylene black and polyvinylidene fluoride (PVDF) in the weight ratio of 80 %, 10 % and 10 %, respectively. Then a few drops of ethanol were added to form a suspension. Subsequently, the slurry was pressed onto nickel foam (Ni Foam) as working electrodes and dried under vacuum at  $60^\circ\text{C}$  for 12 h before test.

### *2.6 Electrode Preparation*

All amperometric experiments were measured with a conventional three-electrode system in 1 M KOH, and the nickel foam (Ni Foam) coating with the as-prepared catalysts were used as the working electrode, a platinum net and a saturated calomel electrode served as the auxiliary

electrode and the reference electrode. The polarization curves of the fabricated electrodes were carried out via CHI660C electrochemical workstation (Shanghai Chenhua Instrument Company, China) with a scan rate of  $2 \text{ mV s}^{-1}$ . The OER activity was recorded by linear sweep voltammetry at a scan rate of  $2 \text{ mV s}^{-1}$  and the stability of the product were record by time-dependent current density for 10 h. Unless stated otherwise, the potential values were standardized with the reversible hydrogen electrode (RHE) using the following equation:  $E(\text{RHE})=E(\text{SCE})+1.07 \text{ V}$ . To bubble away the surface contaminants and stabilize the working electrode, the fabricated electrodes should be preprocessed under a continuous Ar flow via cyclic voltammetry for at least 400 cycles.

### 3. Results and discussion

In a typical approach, the prepared PVP NFs containing the La, Sr, Co and Mn salt (LSCM/PVP NFs) were firstly prepared through the electrospinning technology. As shown in Fig. S1. The LSCM/PVP NFs exhibit distinct fibrous morphology with smooth surfaces and the nanofiber diameters range from 300 to 500 nm. After calcination in air for 3 h, the pre-formed LSCM/PVP NFs were converted into LSCM NFs with unique hollow and porous structures. As illustrated in Fig. 1a, the inside tube diameters of LSCM NFs range from 100-200 nm and the LSCM NFs range from hundreds of nanometers to dozens of micrometers in the length. And the specific surface area of the LSCM is calculated to be about  $36.64 \text{ m}^2 \text{ g}^{-1}$  (Fig. S2) via Brunauer-Emmett-Teller (BET) method, which is larger than the present report perovskite materials [45,46]. Fig. 1b indicates that the LSCM NFs possess rough surfaces and porous structures. Large amounts of the small LSCM NPs served as building blocks and connected with each NPs to form the whole hollow LSCM NFs. The diameter of the LSCM NPs is about  $20 \pm 4 \text{ nm}$  (inset in Fig. 1b), and the porous structures are beneficial for exposing active sites, which improving

the high OER activity. Fig. 2c displays the high-resolution transmission electron microscopy (HRTEM) image of the LSCM NPs and it indicates the visible interplanar spacing of 3.8 Å and 2.7 Å, corresponding to (012) and (110) planes of  $\text{La}_{0.7}\text{Sr}_{0.3}\text{Co}_{0.25}\text{Mn}_{0.75}\text{O}_3$  NPs. And the results of TEM-EDS indicate that the LSCM have a formula of  $\text{La}_{0.7}\text{Sr}_{0.3}\text{Co}_{0.25}\text{Mn}_{0.75}\text{O}_3$  (Fig. S3). The selected area electron diffraction (SAED) pattern (inset in Fig. 1c) exhibits the regular polycrystalline ring corresponding to the (024), (030) and (134) planes of the  $\text{La}_{0.7}\text{Sr}_{0.3}\text{Co}_{0.25}\text{Mn}_{0.75}\text{O}_3$  NPs. Fig. 1d exhibits the line-scan EDX spectra of the cross section of LSCM NFs, and it is indicated that the La, Sr, Co, Mn and O signals were mainly centered at the edges of NFs, which are stronger than those in the inner NFs, confirming the formation of hollow structure. The STEM-EDS (Fig. 1g-k) mapping images of LSCM NFs display the well distribution of La, Sr, Co, Mn and O elements, further suggesting the successfully fabrication of “all-in-one” multi-element perovskite oxides.

X-ray photoelectron spectroscopy (XPS) was used to further investigate the chemical states of LSCM NFs (Fig. 2). The La 3d XPS spectrum of LSCM NFs exhibits two distinct peaks located at 833.8 and 837.9 eV, corresponding to the La 3d<sub>5/2</sub> and its shake-up satellite respectively, which has concluded the predominant state of La (III) in the complex oxide (Fig. 2a) [46,48,49]. The Sr 3d XPS spectrum displays two significantly peaks located at 133.6 and 132.0 eV, which are attributed to the Sr 3d<sub>5/2</sub> of the Sr<sup>2+</sup> (Fig. 2b) [46,50-52]. As illustrated in Fig. 2c, the characteristic peaks located at 795.8 and 780.5 eV can be assigned to Co 2p<sub>3/2</sub> and Co 2p<sub>1/2</sub>, confirming the presence of Co<sup>2+</sup> ions. The satellite peaks and the other peak located at 789.1 eV belong to the trivalent Co ions [30,53]. For Mn 2p XPS spectra (Fig. 2d), there are three pairs of peaks for Mn 2p<sub>3/2</sub> and Mn 2p<sub>1/2</sub>. The first pair of peaks are located at 652.7 and 641.4 eV, corresponding to the Mn 2p<sub>3/2</sub> and Mn 2p<sub>1/2</sub> of Mn<sup>2+</sup>. The peaks located at 653.8 and 643.9 eV

correspond to Mn  $2p_{3/2}$  and Mn  $2p_{1/2}$ , revealing that the surface Mn species exhibit approximately 3.0+ in the oxidation state. Besides, the peaks located at 655.3 and 642.4 eV relate to the Mn  $2p_{3/2}$  and Mn  $2p_{1/2}$  of Mn<sup>4+</sup> [30,54]. Fig. 2e indicates the O 1s XPS spectra, and the peaks located at 532.6 and 531.2 eV correspond to the residual oxygen containing group and the hydroxyl groups or the surface adsorbed oxygen. The peak with binding energy of 529.0 eV belongs to the lattice oxygen species [55,56]. The XPS results indicate the successfully fabrication of “all-in-one” multi-element perovskite oxides hollow nanofibers. X-Ray diffraction (XRD) pattern was used to investigate the crystal structures of the hollow LSCM NFs (Fig. 2f). The hollow LSCM NFs exhibit a series of characteristic peaks located at 22.9 °, 32.5 °, 40.2 °, 46.9 °, 52.7 °, 58.1 °, 68.8 ° and 77.9 °, respectively, corresponding to the (012), (100), (202), (024), (122), (030), (208) and (134) planes of the La<sub>0.7</sub>Sr<sub>0.3</sub>Co<sub>0.25</sub>Mn<sub>0.75</sub>O<sub>3</sub> phase (JCPDS 51-0408).

The hollow and porous structures of LSCM NFs are important factors for the OER catalysis, and therefore, we further investigated the thermo-dependent morphology evolutions controlled by the calcination temperatures and heating rates. The LSCM NFs prepared at 400, 600, 800 and 1000 °C are denoted as LSCM-400, LSCM-600, LSCM-800 and LSCM-1000, respectively. As shown in Fig. 3, with the increased temperatures from 400 to 1000 °C, the LSCM NFs remain the hollow structures. However, the tubular diameters significantly decrease from  $50 \pm 5$  nm to  $10 \pm 5$  nm, and in addition, higher temperature lead to the decrease in the length of LSCM NFs. At 1000 °C, the as-prepared LSCM-1000 NFs exhibit the fractures of the fibrous structure. As shown in Fig. 3a and 3b, the building block LSCM NPs exhibit small sizes and larger amounts of the NPs densely assembled together to form the hollow LSCM NFs.

With increased temperatures to 600 °C, as shown in Fig. 3c and 3d, the LSCM NPs become relative larger with the decrease in the tubular diameter. Form Fig. 3e and 3f, at 800 °C, due to the larger sizes of LSCM NPs, there were larger amounts of pores throughout the NFs, and the boundaries of the NPs are clearly. The hollow and porous structure can expose more active site for the OER and increase the contact area between the catalyst and electrolyte, which is beneficial for promoting the OER process. The increased sizes of the NPs lead to the formation of pores on the surfaces of NFs due to the aggregated NPs side by side. With further increased to 1000 °C, as shown in Fig. 3g and 3h, more and more NPs were merged and the hollow and porous structure can not be maintained.

The above results display morphology evolutions of the LSCM NFs with different calcination temperature at the same heating rate (2 °C min<sup>-1</sup>). Calcination temperature affected the hollow structure, tubular diameters and sizes of building block LSCM NPs. We further investigated the effects of heating rate on the hollow structure and morphologies. Fig. 4 indicated the LSCM NFs prepared at 800 °C with various heating rates from 2 to 20 °C/min. As shown in Fig. 4a and 4b, the LSCM-2 exhibits a typical hollow fiber structure with larger amounts of pores on surfaces. With increased heating rates to 5 and 10 °C/min (Fig. 4c-4f), the sizes of the LSCM NPs further increased and the surfaces of the NFs became relative rougher. When the heating rate is 20 °C min<sup>-1</sup>, the LSCM NFs exhibit sharp contraction with gully-like surfaces and the tubular structures were not obviously as shown in Fig. 4g and 4h. The building block LSCM NPs tend to coalesce with surrounding NPs to form irregular NPs with larger sizes, resulting in the significantly decrease in tubular diameters and specific surface area.

We further investigate the effects of various temperatures and heating rates on the structures and morphologies of LSCM NFs by XRD characterization. Fig. 5a displays the LSCM NFs

prepared at different temperatures with the range from 400 to 1000 °C. Fig. 5b exhibits the LSCM NFs prepared at various heating rates ranged from 2 to 20 °C/min. Both LSCM NFs only exhibit distinct characterized peaks for  $\text{La}_{0.7}\text{Sr}_{0.3}\text{Co}_{0.25}\text{Mn}_{0.75}\text{O}_3$  crystal phase (JCPDS 51-0408), confirming the successful formation of pure phase  $\text{La}_{0.7}\text{Sr}_{0.3}\text{Co}_{0.25}\text{Mn}_{0.75}\text{O}_3$ . In addition, the temperatures and heating rates did not affect the crystal phase of the  $\text{La}_{0.7}\text{Sr}_{0.3}\text{Co}_{0.25}\text{Mn}_{0.75}\text{O}_3$ . The  $2\theta$  degree changes for different samples are summarized in Table S1 and S2. The thermogravimetry (TG) curves indicate that after 400 °C, there were no obvious changes in the weight, further demonstrate the temperature did not affect the crystal phases (Fig. S4).

Unlike with the previous reported perovskite oxides prepared by combining sol-gel and calcination process, the “all-in-one” strategy is facile to synthesize multi-elemental hollow perovskite oxides NFs with controllable tubular structure and morphology by combining the electrospinning technology and Oswald ripen. The growth process of the hollow LSCM perovskite nanofibers is illustrated in Fig. 6, including the formation process of the porous and hollow structure. Generally, Ostwald ripening involves the initial formation of small crystals and the subsequent growth of bigger crystals at the expense of smaller crystals due to the energy difference among them. Consequently, when the larger crystals grow, the area around them is depleted of smaller crystals. In this work, the electrospun precursor fibers are uniform in radial direction and have a smooth surface. In the pre-treated electrospun precursor fibers structure, metallic ions show a decreasing concentration gradient from its surface to the center. When they are applied by the high-temperature heat treatment,  $\text{LaSrCoMnO}$  crystals would favorably be formed in the outer part prior to in the inner one. With the lower temperature, the multi-elemental ions indicate a decreasing concentration gradient from the surface to the center of nanofibers, and a phase transform from metal ions to LSCM perovskite NPs on the surface of the

nanofiber. During the further high temperature heat treatment process, the LSCM perovskite NPs tend to increase the crystallinity and the NPs stacked together to form a hollow structure with abundant pores due to the Ostwald ripen. Therefore, an interior space can be created between the NPs with accurately temperature control, and the architecture and morphologies of the hollow LSCM perovskite NFs can be also engineered. As a result, an interior space is created within the fibers and hollow tubular structures are available.

The multi-elemental hollow LSCM NFs can be used as efficient OER electrocatalysts. To make a thorough inquiry of the catalytic properties of the sample with different prepared conditions, the electrochemical performance for the OER activity were collected in a 1 M KOH solution by using a typical three-electrode system, as well as of pure Ni foam as supported electrode. Obviously, linear sweep voltammetry (LSV) measurements display that the LSCM-800 expresses the lowest onset potential ( $\approx 1.59$  V) with respect to a reversible hydrogen electrode (RHE) among the various perovskite oxides prepared at other temperatures (Fig. 7a). We calculated the overpotentials ( $\eta_{10}$ ) at  $10 \text{ mA cm}^{-2}$  (Fig. 7b) and the current density at overpotential of 420 mV (Fig. 7c) to compare the catalytic performance. The overpotentials ( $\eta_{10}$ ) at  $10 \text{ mA cm}^{-2}$  for Ni foam, LSCM-400, LSCM-600, LSCM-800 and LSCM-1000 are 450, 440, 430, 400, 420 mV, respectively (Fig. 7b). The current densities at overpotential of 420 mV for Ni foam, LSCM-400, LSCM-600, LSCM-800 and LSCM-1000 are 6, 8, 7, 13 and 8  $\text{mA cm}^{-2}$ , respectively (Fig. 7c). Both results indicate the high OER activity of LSCM-800. With the beneficial of the hollow and porous NFs structure, the LSCM NFs electrocatalysts can magnify the possibility of the catalytic sites and accelerate the contact surface between catalyst and electrolyte.

As for the perovskite NFs prepared at 800 °C with different heating rates, the LSV curves were shown in Fig. 7d, the pure Ni foam was used as control. The LSCM-10 hollow perovskite with exhibit the highest catalytic activity with a low onset potential of 1.54 V vs RHE, this value is comparable to that of commercial IrO<sub>2</sub> catalyst ( $\approx$  1.47 V vs RHE) [37,39]. The details of the electrochemistry performance were showed in Fig. 6e and 6f. The overpotentials ( $\eta_{10}$ ) at 10 mA cm<sup>-2</sup> for Ni foam, LSCM-2, LSCM-5, LSCM-10, LSCM-20 are 400, 360, 340, 420, 450 mV (Fig. 7e). The current density at overpotential of 420 mV for Ni foam, LSCM-2, LSCM-5, LSCM-10, LSCM-20 are 13, 26, 36, 9 and 6 mA cm<sup>-2</sup> (Fig. 7f). Therefore, LSCM-10 catalyst manifested the higher activity than pure Ni foam and other perovskite oxides prepared with different temperatures and heating rates. Finally, the LSCM-10 perovskite showed good OH<sup>-</sup> adsorption, as observed by FT-IR spectroscopy (Fig. S5). A broad IR band centered at approximately 3460 cm<sup>-1</sup> corresponding to H-bonded OH stretching vibrations [57,58]. The electrochemical parameters of the LSCM sample prepared at different conditions and Ni foam are arrangement in the Table 1.

It is very important to investigate the stability of the catalysts for the practical applications. From the time-dependent current density of LSCM-10 and IrO<sub>2</sub>(Fig. 7g), it is indicated that the current density of the as-prepared LSCM perovskite remains more stable in the long-term electrochemical process for 10 h than IrO<sub>2</sub>, and only shows a decrease of 10 % in the current density. The inset in Fig. 7g is the photograph of the three electrodes working system, and the surface of the working electrode displays a mass of O<sub>2</sub> bubble during the stability test. To evaluate the catalysts prepared with different conditions durability in alkaline environments, potentiostatic electrolysis cycling was performed at 1.67 vs. RHE for 10 h. As shown in Fig. S6, the result showed that the hollow LSCM NFs exhibit excellent stability and the LSCM-10

display good OER performance. We further characterized catalyst after the long-term stability test using SEM and XRD, as shown in Fig. S7a and S7b. We can conclude that the hollow LSCM NFs electrocatalyst has good stability in both the hollow NFs structure and the crystal structures.

As shown in Fig. 7h, the corresponding Tafel slopes of Ni foam, LSCM-400, LSCM-600, LSCM-800 and LSCM-1000 are 157, 144, 140, 137, 132  $\text{mV dec}^{-1}$ , respectively. In addition, the Tafel slopes of Ni foam, LSCM-2, LSCM-5, LSCM-10 and LSCM-20 are 157, 142, 132, 125 and 111  $\text{mV dec}^{-1}$ , respectively (Fig. 7i). Notably, the hollow LSCM perovskite NFs prepared at 800 °C and 10 °C  $\text{min}^{-1}$  demonstrated the excellent electrocatalytic performance and a long-term stability in alkaline electrolyte. Owing to the hollow, porous structure, and larger specific surface area with more exposed active sites, the as-prepared “all-in-one” multi-element perovskite oxides can be used as a highly active OER catalyst. The comparison of some LSCM samples with the common microstructures OER electrocatalysts is summarized in Table S3, revealing the considerable OER performance of the electrodes synthesized in this work [59-62].

#### 4. Conclusion

In this work, we provided an effective “all-in-one” strategy for the synthesis of hollow multi-element perovskite oxides NFs with controllable tubular structure and morphology by combining the electrospinning technology and Ostwald ripening approach. The LSCM NFs consist of large amounts of building block NPs, forming the unique architecture and the morphologies can be adjusted by changing the calcination temperatures and the heating rates. The OER performance results show that the as-prepared perovskite oxides exhibited excellent OER activity due to the unique architecture of hollow NFs, which generated large specific surface area, a high porosity and a large inner space. This work provided a simple method to create the hollow LSCM

perovskite NFs and the hollow NFs architecture exhibited a large specific surface area, a high porosity and a large inner space, which are beneficial for the OER, reducing the overpotentials and accelerating the electrode kinetics.

### Acknowledgments

This study was supported by the National Natural Science Foundation of China (NSFC) (Grant no. 51573166), the MOE & SAFEA, and 111 Project (B13025).

### REFERENCES

- [1] S. Chu, A. Majumdar, Opportunities and challenges for a sustainable energy future, *Nature* 488 (2012) 294-303.
- [2] V. R. Stamenkovic, D. Strmcnik, P. P. Lopes, N. M. Markovic, Energy and fuels from electrochemical interfaces, *Nat. Mater.* 16 (2017) 57-69.
- [3] B. Y. Xia, Y. Yan, N. Li, H. B. Wu, X. W. D. Lou, X. Wang, A metal-organic framework-derived bifunctional oxygen electrocatalyst, *Nat. Energy* 1 (2016) 15006.
- [4] Q. Wang, T. Hisatomi, Q. X. Jia, H. Tokudome, M. Zhong, C. Z. Wang, Z. H. Pan, T. Takata, M. Nakabayashi, N. Shibata, Y. B. Li, L. D. Sharp, A. Kudo, T. Yamada, K. Domen, Scalable water splitting on particulate photocatalyst sheets with a solar-to-hydrogen energy conversion efficiency exceeding 1, *Nat. Mater.* 15 (2016) 611-615.
- [5] S. Dutta, A review on production, storage of hydrogen and its utilization as an energy resource, *J. Ind. Eng. Chem.* 20 (2014) 1148-1156.
- [6] Y. Ito, W. T. Cong, T. Fujita, Z. Tang, M. W. Chen, High catalytic activity of nitrogen and sulfur Co-doped nanoporous graphene in the hydrogen evolution reaction, *Angew. Chem. Int. Edit.* 54 (2015) 2131-2136.

- [7] S. Dunn, Hydrogen futures: toward a sustainable energy system, *Int. J. Hydrogen Energy* 27 (2002) 235-264.
- [8] Y. M. Kang, Y. J. Gong, Z. J. Hu, Z. W. Li, Z. W. Qiu, X. Zhu, P. M. Ajayan, Z. Y. Fang, Plasmonic hot electron enhanced MoS<sub>2</sub> photocatalysis in hydrogen evolution, *Nanoscale* 7 (2015) 4482-4488.
- [9] Z. Y. Lin, L. H. Li, L. L. Yu, W. J. Li, G. W. Yang, Ag/AgCl plasmonic cubes with ultrahigh activity as advanced visible-light photocatalysts for photodegrading dyes, *J. Mater. Chem. A* 3 (2015) 7649-7658.
- [10] L. Liao, S. N. Wang, J. J. Xiao, X. J. Bian, Y. H. Zhang, M. D. Scanlon, X. L. Hu, Y. Tang, B. H. Liu, H. H. Girault, A nanoporous molybdenum carbide nanowire as an electrocatalyst for hydrogen evolution reaction, *Energy Environ. Sci.* 7 (2014) 387-392.
- [11] Y. Jiao, Y. Zheng, M. Jaroniec, S. Z. Qiao, Design of electrocatalysts for oxygen-and hydrogen-involving energy conversion reactions, *Chem. Soc. Rev.* 44 (2015) 2060-2086.
- [12] H. Zhu, J. F. Zhang, R. P. Yan Zhang, M. L. Du, Q. F. Wang, G. H. Gao, J. D. Wu, G. M. Wu, M. Zhang, B. Liu, J. J. Yao, X. W. Zhang, When cubic cobalt sulfide meets layered molybdenum disulfide: a core-shell system toward synergetic electrocatalytic water splitting, *Adv. Mater.* 27 (2015) 4752-4759.
- [13] M. Gong, W. Zhou, M. C. Tsai, J. G. Zhou, M. Y. Guan, M. C. Lin, B. Zhang, Y. F. Hu, D. Y. Wang, J. Yang, S. J. Pennycook, B. J. Hwang, H. J. Dai, Nanoscale nickel oxide/nickel heterostructures for active hydrogen evolution electrocatalysis, *Nat. Commun.* 5 (2014) 4695.
- [14] Z. W. Seh, J. Kibsgaard, C. F. Dickens, Chorkendorff, J. K. Nørskov, T. F. Jaramillo, Combining theory and experiment in electrocatalysis: Insights into materials design, *Science* 355 (2017) 4998.

- [15] J. Suntivich, K. J. May, H. A. Gasteiger, J. B. Goodenough, Y. Shao-Horn, A perovskite oxide optimized for oxygen evolution catalysis from molecular orbital principles, *Science* 334 (2011) 1383-1385.
- [16] Y. M. Lee, J. Suntivich, K. J. May, E. E. Perry, Y. Shao-Horn, Synthesis and activities of rutile IrO<sub>2</sub> and RuO<sub>2</sub> nanoparticles for oxygen evolution in acid and alkaline solutions, *J. Phys. Chem. Lett.* 3 (2012) 399-404.
- [17] M. R. Gao, W. C. Sheng, Z. B. Zhuang, Q. R. Fang, S. Gu, J. Jiang, Y. S. Yan, Efficient water oxidation using nanostructured  $\alpha$ -nickel-hydroxide as an electrocatalyst, *J. Am. Chem. Soc.* 136 (2014) 7077-7084.
- [18] M. Ledendecker, S. Krick Calderón, C. Papp, H. P. Steinrück, M. Antonietti, M. Shalom, The synthesis of nanostructured Ni<sub>5</sub>P<sub>4</sub> films and their use as a non-noble bifunctional electrocatalyst for full water splitting, *Angew. Chem.* 127 (2015) 12538-12542.
- [19] H. R. Byon, J. Suntivich, Y. Shao-Horn, Graphene-based non-noble-metal catalysts for oxygen reduction reaction in acid, *Chem. Mater.* 23 (2011) 3421-3428.
- [20] Q. Liu, J. Q. Tian, W. Cui, P. Jiang, N. Y. Cheng, A. M. Asiri, X. P. Sun, Carbon nanotubes decorated with CoP nanocrystals: a highly active non-noble-metal nanohybrid electrocatalyst for hydrogen evolution, *Angew. Chem.* 126 (2014) 6828-6832.
- [21] F. Y. Cheng, T. R. Zhang, Y. Zhang, J. Du, X. P. Han, J. Chen, Enhancing electrocatalytic oxygen reduction on MnO<sub>2</sub> with vacancies, *Angew. Chem. Int. Edit.* 52 (2013) 2474-2477.
- [22] J. Wu, Y. Xue, X. Yan, W. S. Yan, Q. M. Cheng, Y. Xie, Co<sub>3</sub>O<sub>4</sub> nanocrystals on single-walled carbon nanotubes as a highly efficient oxygen-evolving catalyst, *Nano Res.* 5 (2012) 521-530.

- [23] M. Hamdani, R. N. Singh, P. Chartier,  $\text{Co}_3\text{O}_4$  and Co-based spinel oxides bifunctional oxygen electrodes, *Int. J. Electrochem. Sci.* 5 (2010) 556-577.
- [24] T. Y. Ma, S. Dai, M. Jaroniec, S. Z. Qiao, Metal-organic framework derived hybrid  $\text{Co}_3\text{O}_4$ -carbon porous nanowire arrays as reversible oxygen evolution electrodes, *J. Am. Chem. Soc.* 136 (2014) 13925-13931.
- [25] H. Han, B. Y. Guan, B. Y. Xia, X. W. Lou, Designed formation of  $\text{Co}_3\text{O}_4/\text{NiCo}_2\text{O}_4$  double-shelled nanocages with enhanced pseudocapacitive and electrocatalytic properties, *J. Am. Chem. Soc.* 137 (2015) 5590.
- [26] S. Chen, S. Z. Qiao, Hierarchically porous nitrogen-doped graphene- $\text{NiCo}_2\text{O}_4$  hybrid paper as an advanced electrocatalytic water-splitting material, *ACS Nano* 7 (2013) 10190-10196.
- [27] X. H. Gao, H. X. Zhang, Q. G. Li, X. G. Yu, Z. L. Hong, X. W. Zhang, C. D. Liang, Z. Lin, Hierarchical  $\text{NiCo}_2\text{O}_4$  Hollow microcuboids as bifunctional electrocatalysts for overall water-splitting, *Angew. Chem. Int. Edit.* 55 (2016) 6290-6294.
- [28] J. Du, C. C. Chen, F. Y. Cheng, J. Chen, Rapid synthesis and efficient electrocatalytic oxygen reduction/evolution reaction of  $\text{CoMn}_2\text{O}_4$  nanodots supported on graphene, *Inorg. Chem.* 54 (2015) 5467-5474.
- [29] J. J. Shi, K. X. Lei, W. Y. Sun, F. J. Li, F. Y. Cheng, J. Chen, Synthesis of size-controlled  $\text{CoMn}_2\text{O}_4$  quantum dots supported on carbon nanotubes for electrocatalytic oxygen reduction/evolution, *Nano Res.* 10 (2017) 3836-3847.
- [30] H. Zhu, D. N. Yu, S. G. Zhang, J. W. Chen, W. B. Wu, M. Wan, L. N. Wang, M. Zhang, M. L. Du, Morphology and structure engineering in nanofiber reactor: tubular hierarchical integrated networks composed of dual phase octahedral  $\text{CoMn}_2\text{O}_4$ /carbon nanofibers for water oxidation, *Small* 13 (2017).

- [31] B. C. Weng, F. H. Xu, C. L. Wang, W. W. Meng, C. R. Grice, Y. F. Yan, A layered  $\text{Na}_{1-x}\text{Ni}_y\text{Fe}_{1-y}\text{O}_2$  double oxide oxygen evolution reaction electrocatalyst for highly efficient water-splitting, *Energy Environ. Sci.* 10 (2017) 121-128.
- [32] W. T. Hong, M. Risch, K. A. Stoerzinger, Toward the rational design of non-precious transition metal oxides for oxygen electrocatalysis, *Energy Environ. Sci.* 8 (2015) 1404-1427.
- [33] H. S. Min, H. W. Park, U. L. Dong, M. G. Park, Z. W. Chen, Design of highly active perovskite oxides for oxygen evolution reaction by combining experimental and ab initio studies, *ACS Catal.* 5 (2015) 150601163246005.
- [34] G. Chen, W. Zhou, D. Q. Guan, J. Sunarso, Y. P. Zhu, X. F. Hu, W. Zhang, Z. P. Shao, Two orders of magnitude enhancement in oxygen evolution reactivity on amorphous  $\text{Ba}_{0.5}\text{Sr}_{0.5}\text{Co}_{0.8}\text{Fe}_{0.2}\text{O}_{3-\delta}$  nanofilms with tunable oxidation state, *Sci. Adv.* 2017, 3 (2017) 1603206.
- [35] J. W. Nai, Y. G. Bu, Y. Le, X. W. Lou, Oriented assembly of anisotropic nanoparticles into frame-like superstructures, *Sci. Adv.* 3 (2017) 1700732.
- [36] A. Grimaud, K. J. May, C. E. Carlton, A. Grimaud, J. Suntivich, Y. Shao-Horn, Double perovskites as a family of highly active catalysts for oxygen evolution in alkaline solution, *Nature Commun.* 4 (2013) 2439.
- [37] K. J. May, C. E. Carlton, K. A. Stoerzinger, M. Risch, J. Suntivich, Y. L. Lee, A. Grimaud, Y. Shao-Horn, Influence of oxygen evolution during water oxidation on the surface of perovskite oxide catalysts, *J. Phys. Chem. Lett.* 3 (2012) 3264-3270.
- [38] W. Zhou, M. W. Zhao, F. L. Liang, S. C. Smith, Z. H. Zhu, High activity and durability of novel perovskite electrocatalysts for water oxidation, *Mater. Horiz.* 2 (2015) 495-501.

- [39] J. Suntivich, H. A. Gasteiger, N. Yabuuchi, H. Nakanishi, J. B. Goodenough, Y. Shao-Horn, Design principles for oxygen-reduction activity on perovskite oxide catalysts for fuel cells and metal–air batteries, *Nature Chem.* 3 (2011) 546-550.
- [40] W. G. Hardin, J. T. Mefford, D. A. Slanac, B. B. Patel, X. Q. Wang, S. Dai, X. Zhao, R. S. Ruoff, K. P. Johnston, K. J. Stevenson, Tuning the electrocatalytic activity of perovskites through active site variation and support interactions, *Chem. Mater.* 26 (2014) 3368-3376.
- [41] J. Zhao, Y. C. Zou, X. X. Zou, T. Y. Bai, Y. P. Liu, R. Q. Gao, D. J. Wang, G. D. Li, Self-template construction of hollow  $\text{Co}_3\text{O}_4$  microspheres from porous ultrathin nanosheets and efficient noble metal-free water oxidation catalysts, *Nanoscale* 6 (2014) 7255-7262.
- [42] C. Z. Zhu, D. Wen, S. Leubner, M. Oschatz, W. Liu, M. Holzschuh, F. Simon, S. Kaskel, A. Eychmüller, Nickel cobalt oxide hollow nanosponges as advanced electrocatalysts for the oxygen evolution reaction, *Chem. Commun.* 51 (2015) 7851-7854.
- [43] J. F. Li, S. L. Xiong, X. W. Li, Y. T. Qian, A facile route to synthesize multiporous  $\text{MnCo}_2\text{O}_4$  and  $\text{CoMn}_2\text{O}_4$  spinel quasi-hollow spheres with improved lithium storage properties, *Nanoscale* 5 (2013) 2045-2054.
- [44] G. R. Yang, X. Xu, W. Yan, H. H. Yang, S. J. Ding, Single-spinneret electrospinning fabrication of  $\text{CoMn}_2\text{O}_4$  hollow nanofibers with excellent performance in lithium-ion batteries, *Electrochimica Acta* 137 (2014) 462-469.
- [45] H. G. Wang, S. Yuan, D. L. Ma, X. B. Zhang, J. M. Yan, Electrospun materials for rechargeable batteries: from structure evolution to electrochemical performance, *Energy Environ. Sci.* 8 (2015) 1660-1681.

- [46] K. Huang, X. F. Chu, L. Yuan, W. C. Feng, X. F. Wu, X. Y. Wang, S. H. Feng, Engineering the surface of perovskite  $\text{La}_{0.5}\text{Sr}_{0.5}\text{MnO}_3$  for catalytic activity of CO oxidation, *Chem. Commun.* 50 (2014) 9200-9203.
- [47] S. Y. Bie, Y. Q. Zhu, J. M. Su, C. Jin, S. H. Liu, R. Z. Yang, J. Wu, One-pot fabrication of yolk-shell structured  $\text{La}_{0.9}\text{Sr}_{0.1}\text{CoO}_3$  perovskite microspheres with enhanced catalytic activities for oxygen reduction and evolution reactions, *J. Mater. Chem. A* 3 (2015) 22448-22453.
- [48] J. M. Christ, C. Ngo, T. Batson, C. A. Cadigan, J. H. Tong, R. M. Richards, R. O'Hayre, S. Pylypenko, Synthesis of high surface area  $\text{Ca}_x\text{La}_{(1-x)}\text{Al}_{(1-x)}\text{Mn}_x\text{O}_{(3-\delta)}$  perovskite oxides for oxygen reduction electrocatalysis in alkaline media, *Catal. Sci. Technol.* 6 (2016) 7744-7751.
- [49] A. E. Maegli, T. Hisatomi, E. H. Ota, S. Yoon, S. Pokrant, M. Grätzel, A. Weidenkaff, Structural and photocatalytic properties of perovskite-type  $(\text{La}, \text{Ca}) \text{Ti} (\text{O}, \text{N})_3$  prepared from A-site deficient precursors, *J. Mater. Chem.* 22 (2012) 17906-17913.
- [50] S. B. Hammouda, F. P. Zhao, Z. Safaei, V. Srivastava, D. L. Ramasamy, S. Iftikhar, S. Kalliola, M. Sillanpää, Degradation and mineralization of phenol in aqueous medium by heterogeneous monopersulfate activation on nanostructured cobalt based-perovskite catalysts  $\text{ACoO}_3$ , (A = La, Ba, Sr and Ce): Characterization, kinetics and mechanism study, *Appl. Catal. B Environ.* 215 (2017) 60-73.
- [51] M. R. Hao, Y. Liu, X. L. Cui, F. He, Y. N. Qing, XPS characterization of nanometer  $\text{LaCoO}_{3-\delta}$  and  $\text{La}_{1-x}\text{Sr}_x\text{CoO}_{3-\delta}$  *J. Fuel Cell Sci. Tech.* 1999 27 (1999) 312-313.
- [52] Poggini L, Ninova S, Graziosi P, Mannini, V. Lanzilotto, B. Cortigiani, L. Malavolti, F. Borgatti, U. Bardi, F. Totti, I. Bergenti, V. A. Dediu, R. Sessoli A combined ion scattering,

- photoemission, and DFT investigation on the termination layer of a  $\text{La}_{0.7}\text{Sr}_{0.3}\text{MnO}_3$  spin injecting electrode *J. Phys. Chem. C* 118 (2014) 13631-13637.
- [53] R. J. Zou, K. B. Xu, T. Wang, G. J. He, Q. Liu, X. J. Liu, Z. Y. Zhang, J. Q. Hu, Chain-like  $\text{NiCo}_2\text{O}_4$  nanowires with different exposed reactive planes for high-performance supercapacitors, *J. Mater. Chem. A* 1 (2013) 8560-8566.
- [54] F. L. Lai, Y. E. Miao, Y. P. Huang, T. S. Chung, T. X. Liu, Flexible hybrid membranes of  $\text{NiCo}_2\text{O}_4$ -doped carbon nanofiber@ $\text{MnO}_2$  core-sheath nanostructures for high-performance supercapacitors, *J. Phys. Chem. C* 119 (2015) 13442-13450.
- [55] X. B. He, F. X. Yin, Y. H. Li, H. Wang, J. N. Chen, Y. H. Wang, B. H. Chen,  $\text{NiMnO}_3/\text{NiMn}_2\text{O}_4$  oxides synthesized via the aid of pollen: ilmenite/spinel hybrid nanoparticles for highly efficient bifunctional oxygen electrocatalysis, *ACS Appl. Mater. Inter.* 8 (2016) 26740-26757.
- [56] H. Xia, J. K. Feng, H. L. Wang, M. O. Lai, L. Lu,  $\text{MnO}_2$  nanotube and nanowire arrays by electrochemical deposition for supercapacitors, *J. Power Sources* 195 (2010) 4410-4413.
- [57] Y. L. Zhu, W. Zhou, Z. G. Chen, Y. B. Chen, C. Su, M. O. Tadé, Z. P. Shao,  $\text{SrNb}_{0.1}\text{Co}_{0.7}\text{Fe}_{0.2}\text{O}_{3-\delta}$  perovskite as a next-generation electrocatalyst for oxygen evolution in alkaline solution, *Angew. Chem. Int. Edit.* 54 (2015) 3897-3901.
- [58] X. M. Xu, C. Su, W. Zhou, Y. L. Zhu, Y. B. Chen, Z. P. Shao, Co-doping strategy for developing perovskite oxides as highly efficient electrocatalysts for oxygen evolution reaction, *Adv. Sci.* 3 (2016).
- [59] B. Q. Li, C. Tang, H. F. Wang, X. L. Zhu, Q. Zhang, An aqueous preoxidation method for monolithic perovskite electrocatalysts with enhanced water oxidation performance, *Sci. Adv.* 2 (2016) 1600495-1600495.

- [60] K. Elumeeva, J. Masa, F. Tietz, F. Yang, W. Xia, M. Muhler, W. Schuhmann, A simple approach towards high-performance perovskite-based bifunctional oxygen electrocatalysts, *ChemElectroChem* 3 (2016) 138 – 143.
- [61] C. Su, W. Wang, Y. Chen, G. Yang, X. Xu, M. O. Tadé, Z. Shao,  $\text{SrCo}_{0.9}\text{Ti}_{0.1}\text{O}_{3-\delta}$  as a new electrocatalyst for the oxygen evolution reaction in alkaline electrolyte with stable performance, *ACS Appl. Mater. Interfaces* 7 (2015) 17663-17670.
- [62] M. Liu, R. Wang, D. F. Li, D. T. Liang, A novel combustion route for the preparation of perovskite-type oxygen permeable materials, *Mater. Chem. Phys.* 102 (2007) 132-139.

## Figure Captions:

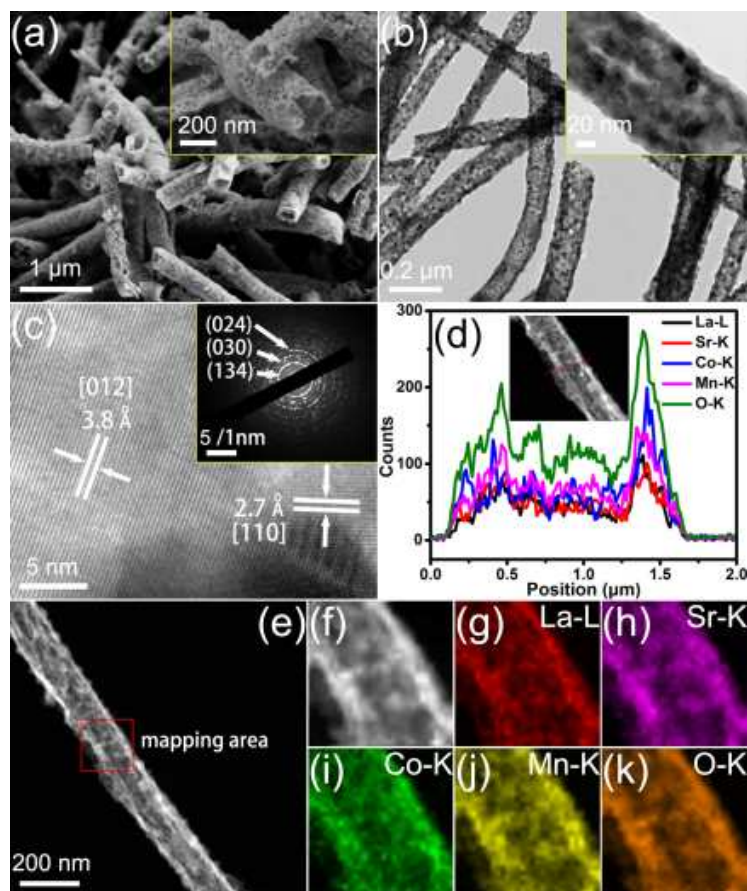


**Fig. 1.** (a) FE-SEM image, (b) TEM image and (c) HRTEM image of the LSCM NFs prepared at 800 °C and the heating rate is 2 °C min<sup>-1</sup>. Inset in Fig. 1a is the high magnification FE-SEM images. Inset in Fig. 1b is the high magnification TEM image. Inset in Fig. 1c is the SAED pattern. (d) The line-scan EDX spectra of the LSCM NFs, and the inset is the cross section area. (e) The HAADF-STEM image of the LSCM NFs. (f-k) The STEM-EDS mapping images area of LSCM.

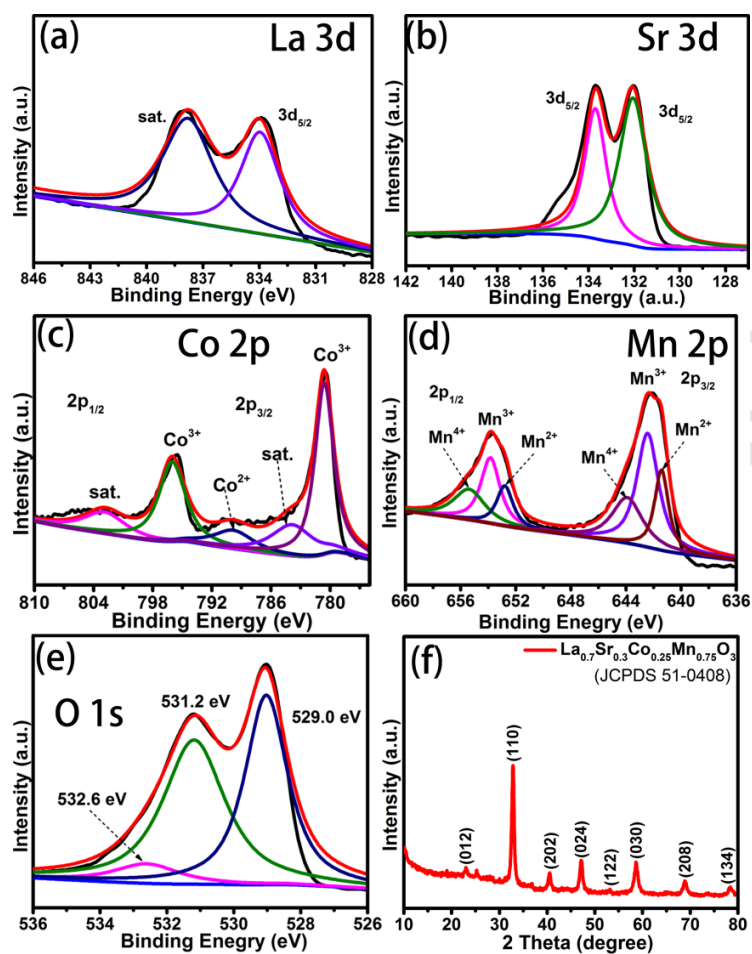


**Fig. 2.** (a) La 3d, (b) Sr 3d, (c) Co 2p, (d) Mn 2p and (e) O 1s XPS spectra of the LSCM NFs. (f) XRD pattern of the LSCM NFs.

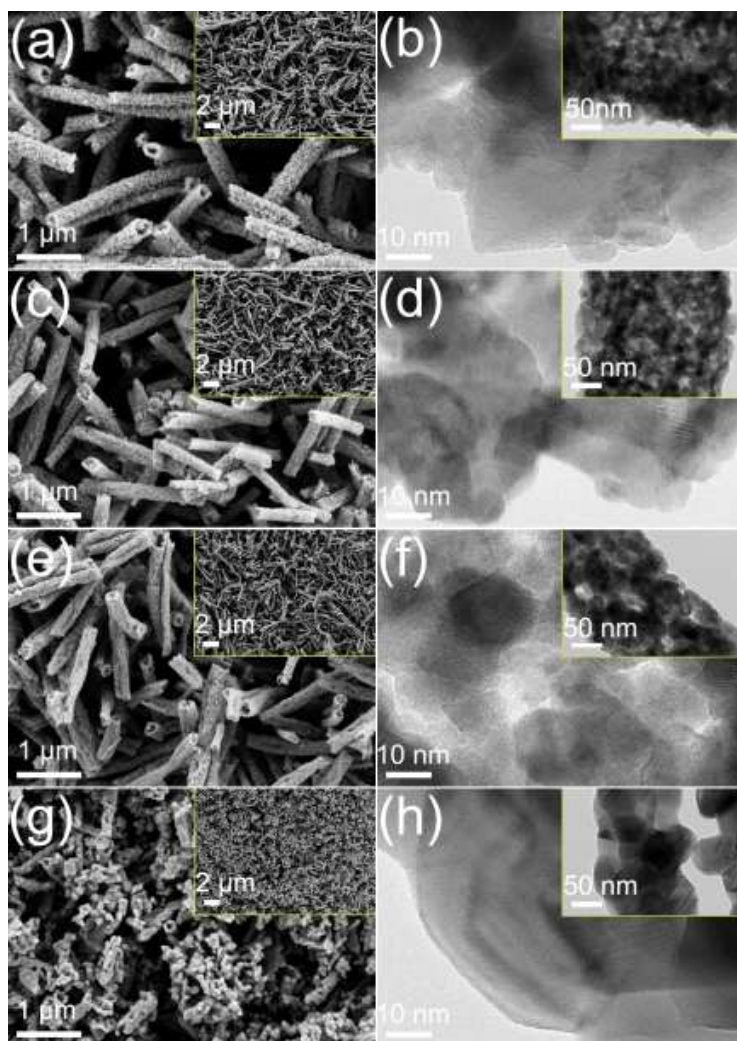


**Fig. 3.** FE-SEM images and the TEM images of the LSCM NFs prepared at different temperatures and heating rate is  $2\text{ }^{\circ}\text{C min}^{-1}$ , (a, b)  $400\text{ }^{\circ}\text{C}$ , (c, d)  $600\text{ }^{\circ}\text{C}$ , (e, f)  $800\text{ }^{\circ}\text{C}$  and (g, h)  $1000\text{ }^{\circ}\text{C}$ .

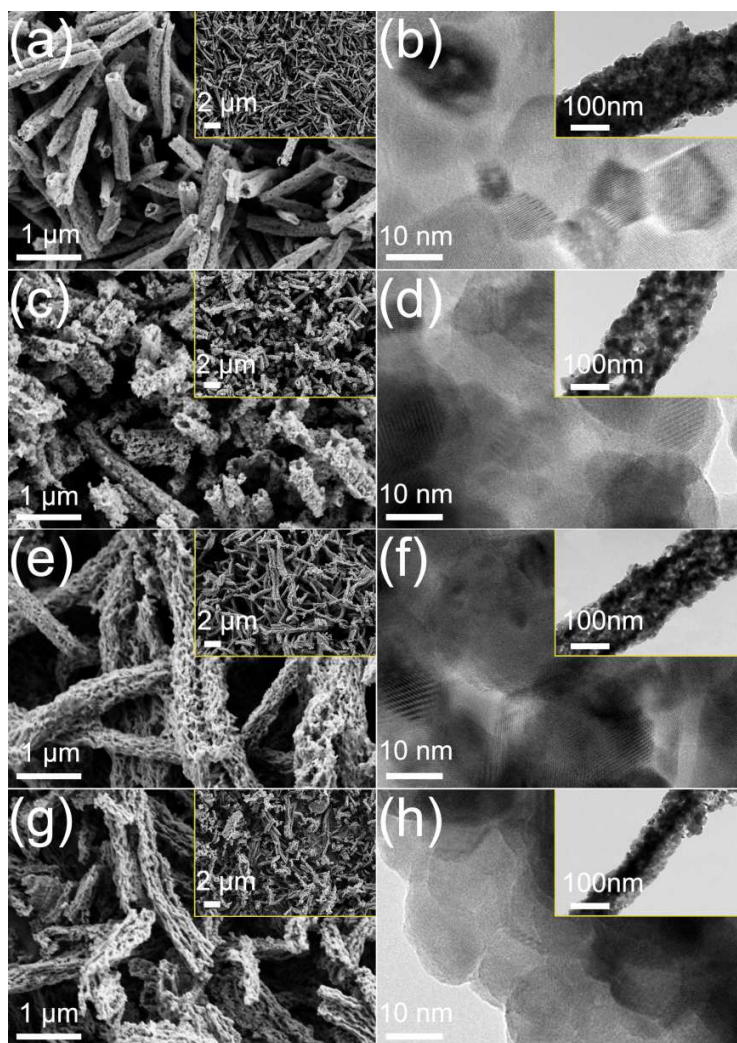


**Fig. 4.** FE-SEM images and the TEM images of the LSCM NFs prepared at 800 °C with various heating rates, (a, b) 2 °C/min, (c, d) 5 °C/min, (e, f) 10 °C/min and (g, h) 20 °C/min.

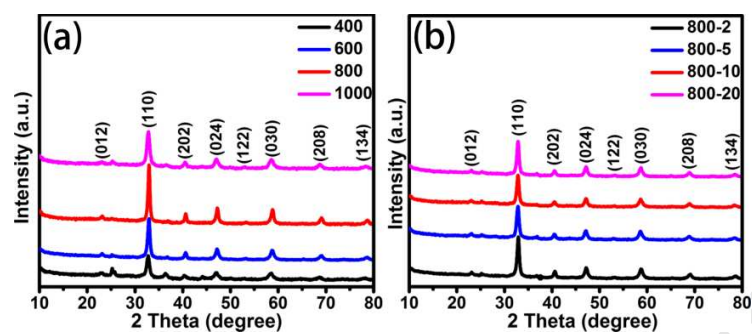


**Fig. 5.** (a, c) XRD pattern patterns of the hollow LSCM NFs prepared at different temperatures with heating rate of 2 °C min<sup>-1</sup>. (b, d) XRD pattern of the hollow LSCM NFs prepared at 800 °C with different heating rates.

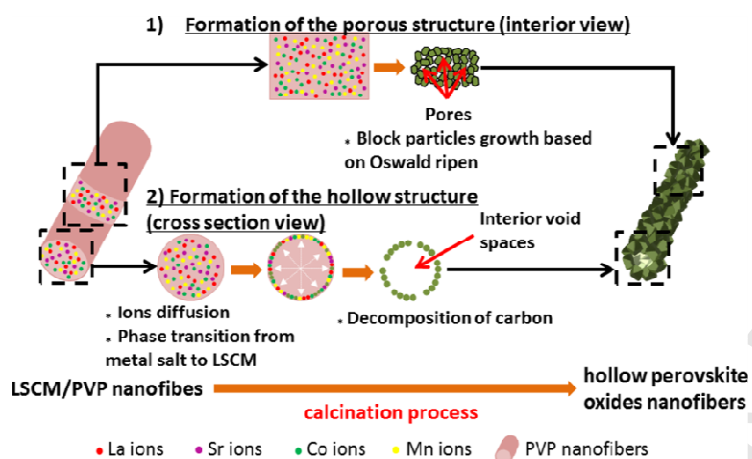


**Fig. 6.** Schematic illustration of the formation mechanism of hollow LSCM NFs.

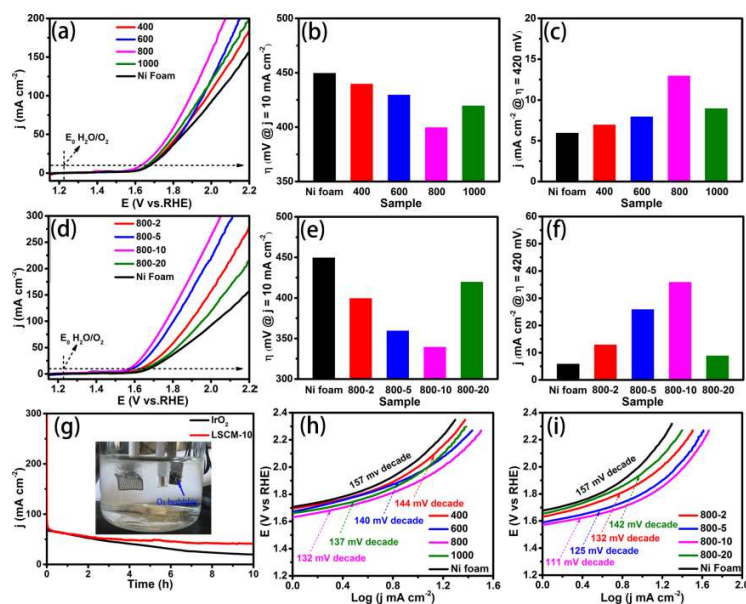


**Fig. 7.** (a) Polarization curves of LSCM NFs prepared at different temperatures on Ni foam in 1.0 M KOH. (b) Overpotentials at the current density of  $10 \text{ mA cm}^{-2}$  for various LSCM NFs prepared at different temperatures on Ni foam. (c) Current density at overpotential of 420 mV for various LSCM NFs prepared at different temperatures. (d) Polarization curves of LSCM NFs prepared at different heating rates on Ni foam in 1.0 M KOH. (e) Overpotentials at the current density of  $10 \text{ mA cm}^{-2}$  for LSCM NFs prepared at different heating rates. (f) Current density at overpotential of 420 mV for LSCM NFs prepared at different heating rates. (g) The time-dependent current density of the LSCM-10 and  $\text{IrO}_2$  at a constant voltage of 1.67 V vs. RHE. The inset in Fig. 7g is the photograph of the  $\text{O}_2$  bubbles formed on the catalysts coated on Ni foam electrode during the electrocatalytic process. (h) The corresponding Tafel plots of LSCM NFs prepared at different temperatures. (i) The corresponding Tafel plots of LSCM NFs prepared at different heating rates.

**Table 1.** Electrochemical Parameters of the LSCM sample prepared at different conditions and Ni foam.

Sample	Onset overpotential (mV)	Overpotential at current density of $10 \text{ mA cm}^{-2}$ (mV)	Current density at $\eta = 420 \text{ mV}$ ( $\text{mA cm}^{-2}$ )	Tafel slopes ( $\text{mV decade}^{-1}$ )
Ni foam	1.66	450	6	157
LSCM-400	1.65	440	7	144
LSCM-600	1.63	430	8	140
LSCM-800	1.59	400	13	132
LSCM-1000	1.65	420	9	137
LSCM-5	1.57	360	26	125
LSCM-10	1.54	340	36	111
LSCM-20	1.62	420	9	142

**Highlights**

- ▶ The multi-elemental perovskite oxides NFs with controllable tubular structure and morphology are synthesized by using electrospinning technology and Ostwald ripening approach.
- ▶ The as-prepared perovskite oxides exhibits excellent OER activity due to the unique architecture of hollow NFs.
- ▶ The LSCM-10 affords overpotential of 340 mV at current density of 10 mA cm<sup>-2</sup> and the Tafel slope is 111 mV dec<sup>-1</sup>.